# Au/Pb Interface Allows the Methane Formation Pathway in Carbon Dioxide Electroreduction

Ahmed Mohsen Ismail, Gergely F. Samu, Huu Chuong Nguyẽn, Edit Csapó, Núria López, and Csaba Janáky*

ABSTRACT: The electrochemical conversion of carbon dioxide (CO_2) to high-value chemicals is an attractive approach to create an artificial carbon cycle. Tuning the activity and product selectivity while maintaining long-term stability, however, remains a significant challenge. Here, we study a series of Au−Pb bimetallic electrocatalysts with different Au/Pb interfaces, generating carbon monoxide (CO), formic acid (HCOOH), and methane (CH_4) as CO_2 reduction products. The formation of CH_4 is significant because it has only been observed on very few Cu-free electrodes. The maximum CH_4 formation rate of 0.33 mA cm^{-2} was achieved when the most Au/Pb interfaces were present. In situ Raman spectroelectrochemical studies confirmed the stability of the Pb native substoichiometric oxide under the reduction conditions on the Au−Pb catalyst, which seems to be a major contributor to CH_4 formation. Density functional theory simulations showed that without Au, the reaction would get stuck on the COOH intermediate, and without O, the reaction would not evolve further than the CHOH intermediate. In addition, they confirmed that the Au/Pb bimetallic interface (together with the subsurface oxygen in the model) possesses a moderate binding strength for the key intermediates, which is indeed necessary for the CH_4 pathway. Overall, this study demonstrates how bimetallic nanoparticles can be employed to overcome scaling relations in the CO_2 reduction reaction.

KEYWORDS: CO$_2$ reduction reaction, solar chemicals, solar fuels, bimetallic catalysts, DFT
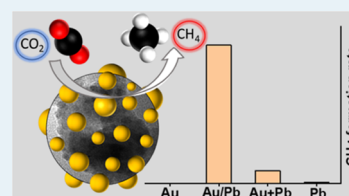
INTRODUCTION

Traditional fossil fuels still occupy a leading position in today's energy structure. Carbon dioxide (CO_2) emissions generated via combustion of fossil energy resources lead to global climate change. Conversion of CO_2 into valuable fuels and chemicals that can act as energy carriers is a promising route to create an artificial and sustainable carbon cycle.[1−3] The electrochemical CO_2 reduction reaction (CO_2RR) is an attractive approach because of its mild operation conditions and the wide range of carbon-based products which can be produced by controlling the reaction conditions. Furthermore, it offers a way to store electricity generated from renewable green energy sources such as solar and wind.[4−6] CO_2RR in an aqueous environment, however, is rather complicated because of substantial kinetic barriers, especially, if we compare to water-splitting.[4] Therefore, developing electrocatalysts with high efficiency, selectivity, and long-term stability is a crucial step of great urgency toward industrialization.[7,8]

The 2e$^-$ products (CO and HCOOH) are rather easy to be produced with high Faradaic efficiency (FE) (close to 100%). Several transition metals (such as Au[9,10] and Ag[11]) and p-block metals (such as Sn[12] and Pb[13]) are good catalysts in this vein. Going beyond 2e$^-$ products is much more challenging. The product distribution on different metal electrodes mostly depends on the binding energy of CO.[14,15] Copper is the only metal having an intermediate binding energy for CO and thus can catalyze the CO_2 reduction to hydrocarbons and alcohols.[16,17] Most Cu surfaces, however, suffer from poor selectivity. A wide range of C_1-C_3 products can be generated, including major products (CO, HCOOH, methane, and ethylene), intermediate products (ethanol, propanol, and allyl alcohol), and minor products (methanol, glycolaldehyde, acetaldehyde, acetic acid, ethylene glycol, propionaldehyde, acetone, and hydroxyacetone).[18] The rich redox chemistry of Cu makes the picture even murkier: the reduction of the partially oxidized layer under electrochemical reduction conditions leads to the formation of defect sites and irreversible reconstruction of the Cu surface, which results in varying catalytic activity and selectivity.[19] For example, a commercial Cu foil showed a total current density of −10 mA cm^{-2} after 2 min of electrolysis, which later declined to −1 mA cm^{-2}. FE$_{CO}$ decreased gradually from 25% during the first hour to 10% over 7 h, and the majority of current was due to the hydrogen evolution reaction (HER).[17]

Moving beyond pure metals, bimetallic nanoparticles (NPs) provide an ideal platform for studying the effect of surface composition[20−25] and to identify how to bypass scaling

relations.[26,27] Through appropriate synthesis procedures, a wide range of combinations (with various compositions, patterns of mixing, and intermetallic phases) can be explored. Such materials can provide multiple active sites for reaction intermediates with tunable binding strength and thus exhibit altered reactivity relative to their monometallic counterparts. Cu-based bimetallic catalysts have been already studied to improve the instability and poor selectivity of Cu as well as to lower the overpotential required to produce multi e$^-$ reduction products.[23,28−31] A few recent studies demonstrated the formation of highly reduced products (>2e$^-$ transfer) using electrocatalysts that do not contain copper. In this vein, nickel (Ni)−gallium (Ga) films with different phases were prepared and tested.[32] Ni_5Ga_3 alloy catalyzed the formation of CH_4, C_2H_4, and C_2H_6 with a total FE of about 4%. Ni_3Al and Ni_3Ga intermetallic compounds also generated C_2 and C_3 products.[33] In another study, the shell thickness dependence of the product distribution was investigated on Pd@Au core−shell NPs. As the thickness of the Pd shell increased from 1 to 10 nm, HCOOH, CH_4, and C_2H_4 were generated in addition to CO and H_2.[34] Finally, it was reported that pulse-deposited Zn dendrites on a Ag foam catalyzed the formation of methanol with a FE $\geq$ 10.5% at a total current density of −2.7 mA cm^{-2}.[35]

Synthesis of bimetallic electrodes containing p-block metals (such as Sn, In, and Pb, all having high H_2 overpotential and favoring HCOOH production) is a good strategy not only to tune the CO_2RR activity and selectivity but also to suppress the HER.[13,36,37] A Sn/SnO_x electrode exhibited 8-fold higher partial current density and 4-fold higher FE for the CO_2RR than the respective Sn foil.[12] Oxide-derived Pb showed up to 700 times lower H^+ reduction activity compared to the Pb foil.[13] Such a low activity was explained by the presence of a thin and metastable surface oxide/hydroxide layer that passivates the surface for HER but is active for CO_2RR over prolonged electrolysis. In our previous work, we highlighted the effect of phase composition of Au−Sn bimetallic NPs on the CO_2RR performance.[20] Two high-value products were formed: HCOOH and syngas with a tunable ratio. The AuSn phase showed the lowest overpotential for the CO_2RR, and Raman spectroelectrochemistry confirmed the generation of formate anions on the AuSn phase at a notably less negative potential compared to the pure Sn electrode.[20] Still, beyond the above examples, the combinations of other p-block metals with Au (as a CO-producing metal) have not been reported as Cu-free catalyst alternatives.

Here, we uncover how the presence of Au/Pb interfaces affect the electrocatalytic activity of Au-decorated Pb bimetallic NPs toward CO_2 reduction. Most importantly, the formation of CH_4 was demonstrated on the Au−Pb catalysts unlike on Au, Pb, or even their physical mixture. Both experimental studies and density functional theory (DFT) simulations indicated that the presence of (subsurface) oxygen associated with Pb together with the existence of the Pb/Au interface are crucial to provide proper sites along the pathway for the CO_2 conversion to CH_4.

■ EXPERIMENTAL SECTION

Materials. Gold(III) chloride trihydrate ($HAuCl_4 \cdot 3H_2O$, 99.9%, Aldrich), lead(II) nitrate [$Pb(NO_3)_2$, $\geq$99.0%, AnalaR NORMAPUR, Reag. Ph. Eur., ACS], sodium citrate dihydrate ($C_6H_5Na_3O_7 \cdot 2H_2O$ 99%, Aldrich), polyvinylpyrrolidone (PVP, M_W = 40,000, Aldrich), L-ascorbic acid ($C_6H_8O_6$ $\geq$99%, ACS

reagent), and sodium borohydride ($NaBH_4$, 99%, Aldrich) were employed without further purification in the different syntheses. The isotopic labeling studies were carried out with carbon dioxide ($^{13}CO_2$, 99 at. % ^{13}C, Sigma-Aldrich) and potassium hydrogen carbonate ($KH^{13}CO_3$, 98 at. % ^{13}C, <3 atom % ^{18}O, Sigma-Aldrich). Milli-Q ultrapure water was used to make all solutions.

Synthesis of Au-Decorated Pb NPs (Au−Pb NPs). A new protocol was developed for the synthesis of Au−Pb bimetallic NPs with different nominal compositions (i.e., Au_5Pb_{95}, $Au_{20}Pb_{80}$, and $Au_{50}Pb_{50}$) using a two-step synthesis approach, starting with the formation of metallic Pb NPs, which act as nucleation seeds, followed by the reduction of the Au precursor. In a typical procedure for the synthesis of $Au_{50}Pb_{50}$, 0.05 g of $Pb(NO_3)_2$ was added to 30 cm^3 of (0.25 mM) PVP. The solution was stirred under a nitrogen atmosphere in a 100 cm^3 round-bottomed flask for 20 min. Subsequently, 20 cm^3 (50 mM) of $NaBH_4$ was added using a syringe pump at a rate of 0.2 cm^3 min^{-1}. The solution was stirred for another 1 h to complete the reaction and decompose the remaining $NaBH_4$. Next, 6 cm^3 (100 mM) of ascorbic acid was added, and the mixture temperature was adjusted to 50 °C. Then, 30 cm^3 of (5 mM) $HAuCl_4$ solution was injected using a syringe pump at a rate of 0.2 cm^3 min^{-1}. The solution was left stirring for 30 min and then allowed to cool down. The product was collected by centrifugation at 10,000 rpm for 20 min and washed with ethanol/water mixture and then dried under nitrogen. Other compositions of Au−Pb bimetallic NPs were synthesized by changing the amount of Au precursor.

Synthesis of Au NPs. Au NPs were prepared using an adopted method.[22] Briefly, 100 cm^3 (0.25 mM) of $HAuCl_4$ solution was heated to boiling under moderate stirring. Then, 0.7 cm^3 of 0.23 M sodium citrate was added, and the solution color turned to wine red within a few seconds. The solution was boiled for a further 15 min and then allowed to cool down to room temperature.

Synthesis of Pb NPs. For the preparation of Pb NPs, 0.09 g of $Pb(NO_3)_2$ and 0.5 g PVP were added to 50 cm^3 of ultrapure water in a 100 cm^3 round-bottomed flask. The solution was stirred under a nitrogen atmosphere for 20 min. Subsequently, 40 cm^3 (50 mM) of $NaBH_4$ was added using a syringe pump at a rate of 0.2 cm^3 min^{-1}. The solution was stirred for another 30 min to complete the reaction. The product was collected by centrifugation at 9000 rpm for 20 min and washed with ethanol and then dried under nitrogen.

Synthesis of Pb-Decorated Au NPs ($Pb_{95}Au_5$ NPs). PVP (0.5 g) was added to 50 cm^3 (0.25 mM) of premade Au NPs in a 250 cm^3 round-bottomed flask and stirred at room temperature for 4 h. Then, 2 cm^3 of 0.14 M $Pb(NO_3)_2$ was added and stirred under nitrogen. After 30 min, 30 cm^3 of (50 mM) of $NaBH_4$ was added using a syringe pump at a rate of 0.2 cm^3 min^{-1}. The stirring was continued for an additional 1 h; then, the particles were collected by centrifugation at 10,000 rpm for 20 min and washed with ethanol/water mixture and then dried under nitrogen. A detailed description of the synthesis of Au seeds is given in the Supporting Information.

Physical Characterization. X-ray diffraction (XRD) patterns were obtained by a Bruker D8 ADVANCE X-ray diffractometer using Cu Kα (λ = 1.5418 Å) radiation in the 2θ range of 10−80° with a scan rate of 0.4° min^{-1}. Transmission electron microscopy (TEM) images were collected on a FEI Tecnai G^2 20 X-Twin microscope working at an accelerating
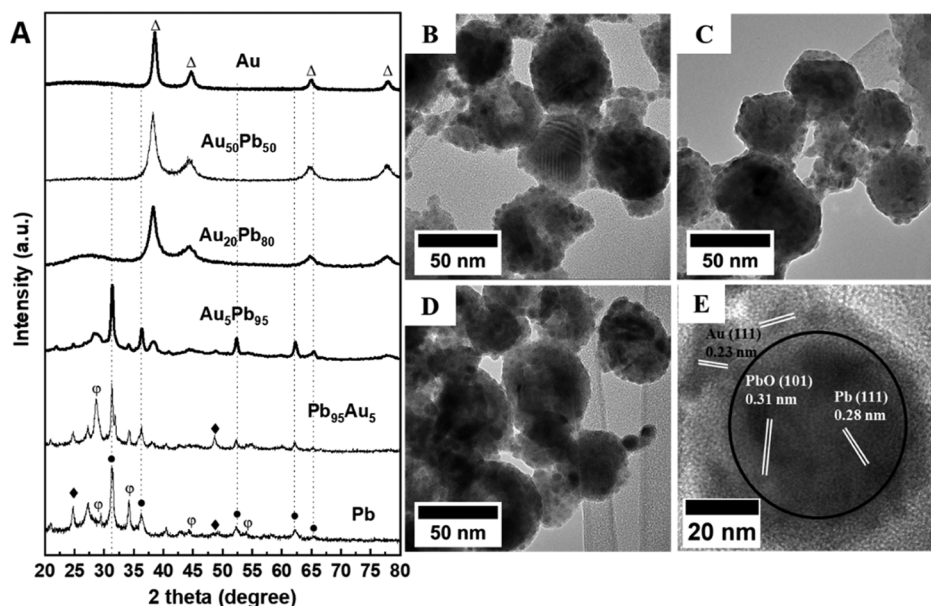
Figure 1. (A) XRD patterns of Au−Pb NPs and the parent metals. These marks indicate the diffractions corresponding to the respective crystal phases in the samples: (diamond solid) α-PbO$_2$ (JCPDS no. 75-2414), (phi) α-PbO (JPDS no. 78-1666), (circle solid) Pb (dot line) (JCPDS no. 02-0799), and (delta) Au (JCPDS no. 04-0784). TEM images of (B) Au$_5$Pb$_{95}$, (C) Au$_{20}$Pb$_{80}$, (D) Au$_{50}$Pb$_{50}$ NPs, and (E) single particle of Au$_5$Pb$_{95}$, showing lattice fringes with a d spacing of 0.23 nm corresponding to the (111) plane of face-centered cubic Au, which are located around a core, that features lattice fringes with a d spacing of 0.31 and 0.28 nm corresponding to (101) and (111) planes of α-PbO and Pb, respectively. The nominal compositions were used for the notation of the Au−Pb bimetallic system.

voltage of 200 kV. A scanning electron microscope (SEM, Hitachi S-4700 field emission) equipped with an energy-dispersive X-ray (EDX) unit was used for elemental analysis. X-ray photoelectron spectroscopy (XPS) was performed with a SPECS instrument equipped with a PHOIBOS 150 MCD 9 hemispherical analyzer. The analyzer was in the FAT mode with 20 eV pass energy. The Al Kα radiation ($h\nu$ = 1486.6 eV) of a dual anode X-ray gun was used as an excitation source and operated at 150 W power. Ten scans were averaged to get a single high-resolution spectrum. Charge neutralization was carried out during spectra acquisition, where the position and width of the adventitious carbon peak were monitored. The adventitious carbon peak was at 284.8 eV in all cases. Ar$^+$ sputtering was carried out to remove the upper layers of the sample, where specified. The Ar$^+$ ion gun was operated at 1.2 kV for 10 min. For spectrum evaluation, CasaXPS commercial software package was used.

Electrode Preparation. Suspensions of the samples were prepared by dispersing the powders in isopropanol (5 mg cm^{-3}). Ultrasonic agitation was used to homogenize the suspension for 30 min. Then, the samples were spray-coated to a preheated (110 °C) glassy carbon electrode using an Alder AD320 type airbrush and a homemade spray-coater robot, operated with 1 bar compressed nitrogen. The obtained layers were subjected to heat treatment in Argon and air atmospheres at 280 °C to alter the quantity of Pb oxide species and to remove any traces of the solvent. The Au-coated electrodes were prepared by drop-casting an aqueous concentrated dispersion to a heated glassy carbon electrode (80 °C). A loading of 0.48 mg cm^{-2} was employed in the experiments.

Electrochemical Measurements and Product Analysis. All electrochemical measurements were performed using a Metrohm Autolab PGSTAT204 type potentiostat/galvanostat. A typical three-electrode gastight two-compartment electrochemical cell was used to characterize the catalytic performance, separated by a Nafion-117 proton exchange membrane. A platinum foil (Alfa Aesar, 99.99%) and Ag/AgCl (3 M NaCl) were used as the counter electrode and the reference electrode, respectively. The measured potentials were converted to the reversible hydrogen electrode (RHE) scale using $E_{RHE} = E_{Ag/AgCl} + 0.210$ V $+ 0.0591 \times$ pH. All currents are presented after normalization to the geometric surface area of the electrodes. Each compartment was filled with 0.5 M KHCO$_3$ solution. The cathode compartment had a ~25 cm^3 headspace and contained 35 cm^3 of the electrolyte. Before electrolysis, the electrolyte in each compartment was purged with CO$_2$ gas for 30 min. The pH of the electrolyte was 7.2 after saturation, at the beginning of the measurements. The electrolyte in the cathodic compartment was stirred with a magnetic stirrer at a rate of 1000 rpm. The effluent gas from the headspace of the cathode compartment was fed into the online sampling loop of the gas chromatograph (GC) every 30 min for quantification of gas-phase CO$_2$ reduction products. A SHIMADZU GC-2010 plus instrument (with ShinCarbon ST column) was used, which was equipped with a BID detector. Helium gas (99.9999%) was employed as the carrier gas. The liquid product was collected at the same time when GC analysis was performed and was analyzed by nuclear magnetic resonance spectroscopy (Bruker ADVANCE Neo 500). Phenol and dimethyl sulfoxide were used as internal standards. The one-dimensional ^{1}H spectrum was measured using a solvent presaturation method to suppress the water peak. The area ratio of the formic acid peak to the phenol peak was compared to the standard curve to quantify the formate concentration. FE values were determined from the charge passed to produce each product by dividing it by the total charge.

In Situ Raman Spectroelectrochemistry. Raman spectra were recorded with a SENTERRA II Compact Raman microscope using 532 nm laser excitation wavelength with

2.5 mW power and a 50× objective. In situ electrochemical Raman experiments were performed using an ECC-Opto-Std electrochemical cell (EL-CELL GmbH) equipped with a sapphire window and a potentiostat/galvanostat (Interface 1010E—GAMRY). The spectra were recorded after a 100 s potentiostatic conditioning at each potential. The working electrodes were prepared by spray-coating of 5 mg cm^{-3} suspensions of $Au_{50}Pb_{50}$ and pure Pb NPs in isopropanol to a preheated (110 °C) carbon paper. All catalysts were studied in CO_2-saturated 0.5 M $KHCO_3$ electrolyte.

Theoretical Calculations. DFT calculations were performed with VASP 5.4.4;[38−41] the Perdew−Burke−Ernzerhof[42,43] functional was used with projected augmented wave pseudopotentials[44,45] and an energy cutoff of the plane waves of 450 eV. Bulk calculations were done with a $3 \times 3 \times 3$ k-point sampling, whereas slabs were calculated with $3 \times 3 \times 1$. After geometry optimization of the bulks Au, Pb, Au_2Pb, and $PbAu_2$, slab calculations were performed with dipole corrections, and van der Waals interactions were included with DFT-D2. For each alloy, the low index surfaces (100, 101, 111, 110, and 001) were investigated. The representation of the diluted alloy Au (3%) in the Pb structure was done by substitution of the Pb site with Au. The choice of using a surface with 3% Au concentration in the simulation instead of the experimental 5% was due to the computational efficiency. Oxide contributions were analyzed by adding O either on the surface or subsurface position. Subsequent CO_2 reduction calculations were performed on the most stable surfaces. The computational hydrogen electrode[46−48] was used for modelling the CO_2 reduction[49] and to compute the Gibbs free energies of the reaction. The final results of PbAu 3% are consistent with larger systems on a 2×2 supercell at γ point with an Au island instead of a single atom.

Additional geometrical structures can be seen in the Supporting Information in Figures S21−S28. All structures can be accessed at the ioChem-BD database[50] under the following link: https://10.19061/iochem-bd-1-167.

RESULTS AND DISCUSSION

XRD measurements were carried out to determine the crystal structure of the Au−Pb NPs. Pure Pb showed diffraction peaks at 2θ = 31.36, 36.34, 52.26, 62.26, and 65.33°, corresponding to the face-centered cubic phase of Pb, and peaks at 2θ = 28.68, 35.74, 44.41, and 54.93° for PbO as well as reflections for PbO_2 at 25.43 and 48.88° (Figure 1A). The intensities of Pb, PbO, and PbO_2 peaks decreased notably with increasing Au concentration to 20%, whereas the Au phase became more prevalent on further increasing the Au content (sample $Au_{50}Pb_{50}$). Pure Au exhibited a face-centered cubic phase. Importantly, these bimetallic samples are not alloys (but rather particles containing nanosized domains of both metals); therefore, there is no shift in the reflection positions with an increase of the Au content (unlike e.g., in the case of Ag−Au alloys[22]). Notably, the small relative intensity of the Pb-related diffractions suggests that the majority of these species are present in an amorphous phase (e.g., nonstoichiometric oxide). TEM images of the as-prepared Au−Pb NPs show Au dots that are well-distributed on the surface of the Pb particles (Figure 1B−D), confirming the suggested formation mechanism. The average size of the bimetallic particles was 42 ± 5 nm for all compositions, slightly higher than that of pure Pb NPs 40 ± 3.5 nm (Figures S1 and S2). For the Au_5Pb_{95} sample, which has the lowest Au content, the deposited Au NPs mainly

surround the Pb NPs (Figure 1E). The Au coverage on the top of Pb particles increases with the Au content; thus more Au/Pb interfaces are present (see Figure S3 for high-resolution TEM images). The inverse structure (i.e., Au core, Pb shell, denoted as $Pb_{95}Au_5$) was also prepared with a composition similar to the most Pb-rich sample (Au_5Pb_{95}), and similar crystal phases were identified (see Figure S2A for TEM image).

XPS was employed to characterize the chemical state of the elements on the NP surface. The XPS survey scans show only Pb, Au, O, and C peaks (Figures S4 and S5). The fitting of the high-resolution Pb 4f spectra shows that the native oxide is the predominant lead component on the surface of all four samples (Figure S6). The relative amount of the native Pb oxide (PbO_x) decreased from 94% to 91% to 72% in the series of the samples with increasing Au content (see also Table S1). The $Au_{50}Pb_{50}$ NPs heated in air exhibited only a Pb 4f peak at 138.45 eV (Figure 2) that corresponds to $Pb^{4+/2+}$, which is
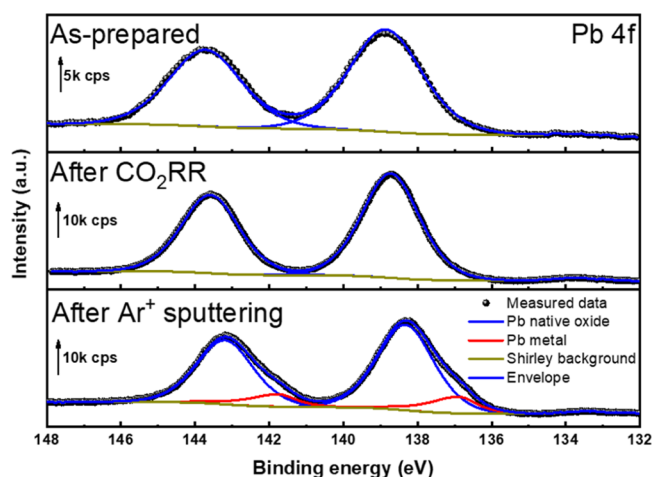

Figure 2. High-resolution XPS spectra of the Pb 4f peaks for the $Au_{50}Pb_{50}$ catalyst before and after CO_2 electrolysis in CO_2-saturated 0.5 M $KHCO_3$ (pH = 7.2) at −1.07 V vs RHE for 1 h and after Ar$^+$ sputtering.

likely due to the native oxide layer.[13] Besides, the lattice oxygen, carbonate, and hydroxide-related oxygen were also detected (see Figure S7). Although discussed in detail below, we mention here that after a 10 h electrolysis experiment, there was no shift in the Pb 4f peak, indicating no change in the oxidation state. The percentage of PbO_x decreased from 77 to 70%, and the Au content increased from 23 to 30%. When mild Ar$^+$ sputtering was employed, the metallic Pb^0 4f peak at 136.86 eV became visible, and the amount of lattice oxygen increased at the expense of carbonate (Figure S7). This confirms the presence of metallic Pb and some nonstoichiometric PbO_x structure beneath the surface layer. EDX data describing the bulk composition are listed in Table S1 together with the surface composition obtained from XPS.

CO_2 electroreduction was investigated first by linear sweep voltammetry (LSV) to identify the onset potential of the electrochemical process. LSV curves were recorded in CO_2-saturated 0.5 M $KHCO_3$ (pH = 7.2) and N_2-saturated 0.5 M Na_2SO_4 (pH = 7.5) to ensure a similar pH. The onset potential recorded in the CO_2-saturated solution was less negative compared to that in the absence of CO_2 (E = −0.73 V in CO_2
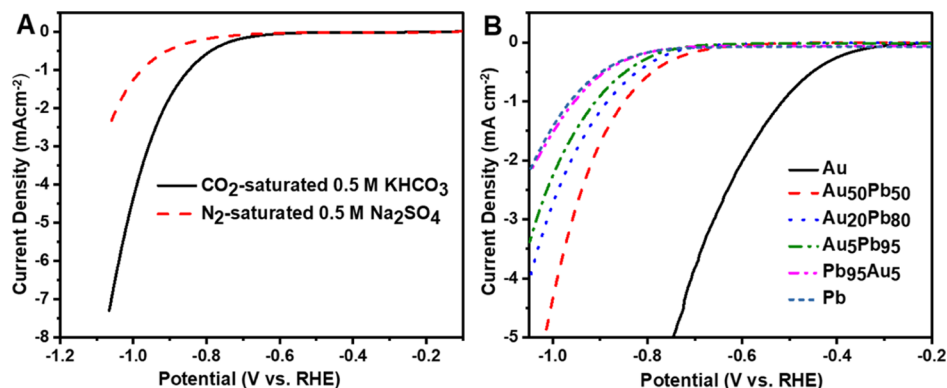
Figure 3. (A) LSV profiles of $Au_{50}Pb_{50}$ catalyst in CO_2-saturated 0.5 M $KHCO_3$ (pH = 7.2) and N_2-saturated 0.5 M Na_2SO_4 (pH = 7.5); scan rate = 5 mV s^{-1}. (B) LSV profiles of Au−Pb NPs with different compositions in CO_2-saturated 0.5 M $KHCO_3$ (pH = 7.2) stabilized after multiple cycles. Scan rate = 5 mV s^{-1}. The layers were heated in the air atmosphere at 280 °C. The loading was 0.48 mg cm^{-2} in all cases.
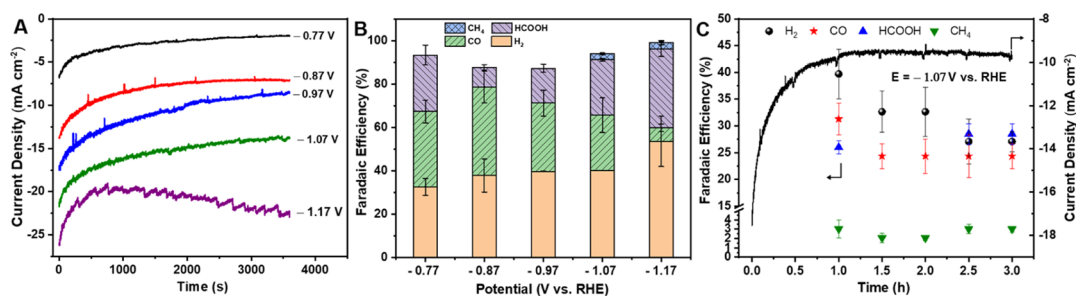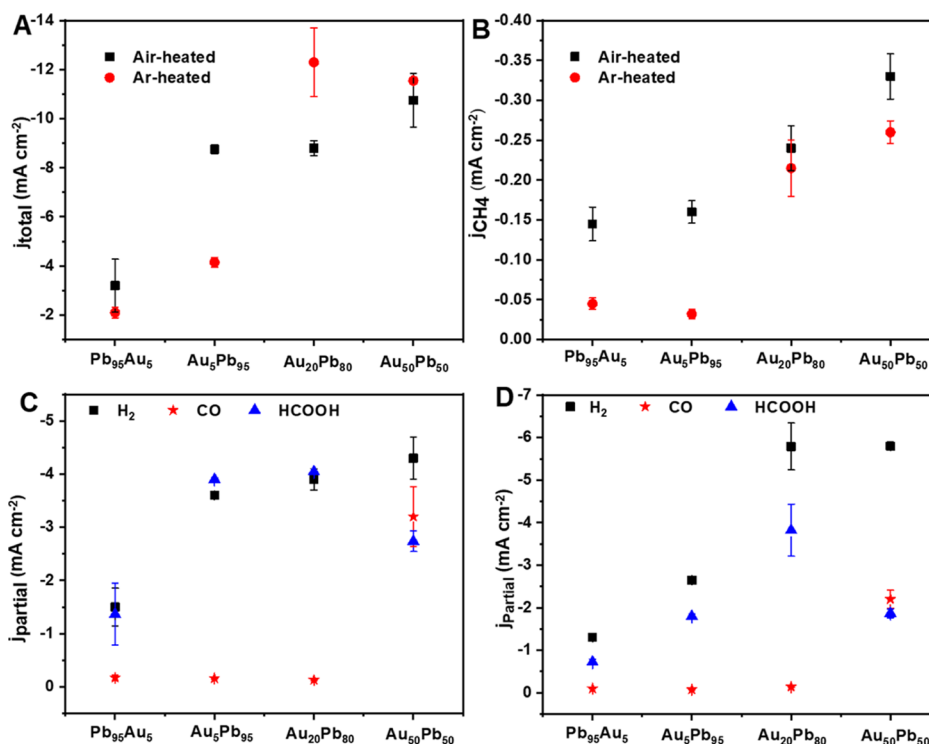

Figure 4. Electrochemical CO_2 reduction activity of the air-heated $Au_{50}Pb_{50}$ catalyst: (A) Total current density as a function of time at various potentials, (B) H_2, CO, HCOOH, and CH_4 FEs of 1 h CO_2 electrolysis at different applied potentials, and (C) 3 h CO_2 electrolysis measured in CO_2-saturated 0.5 M $KHCO_3$ at −1.07 V vs RHE.

vs −0.88 V in N_2 vs RHE, see Figures 3A and S8 and S9). This indicates that in the CO_2-saturated electrolyte, an additional process occurs at a less negative potential besides the HER.[20] The comparison of the voltammetric curves of the different Au−Pb NPs is presented in Figure 3B. There is a well-defined trend in the onset potentials with the change in their composition. The least negative potential was witnessed for Au and the most negative for Pb (all the bimetallic electrodes lied in between). In the case of the samples heat-treated in Ar, no clear trend was observed, and the onset potential values of the Au-rich catalysts ($Au_{50}Pb_{50}$ and $Au_{20}Pb_{80}$) were more negative than those recorded for samples heated in Air (Figure S10). This observation can be rationalized by the catalytically active nature of PbO_x of sites. Cyclic voltammograms (CVs) were also recorded for all samples. For example, CV traces of the $Au_{20}Pb_{80}$ electrode showed the characteristic oxidation and reduction peaks of both Pb and Au, confirming the presence of both elements on the surface (see Figure S11 and discussion therein).

The CO_2 reduction performance of the bimetallic NPs was explored under chronoamperometric conditions. Analysis of the electrolysis products confirmed the formation of CH_4 (highly reduced C_1 product) besides CO and HCOOH, whereas the remaining charge was attributed to the HER. First, we investigated how the potential affects the product distribution. Pure Au produced mainly CO (FE ≥ 70%) with very little dependence on the applied potential, and some minor traces of HCOOH were also detected (Figure S12B). Pure Pb generated HCOOH and H_2, and the maximum FE_{HCOOH} was 78% at −1.07 V versus RHE, whereas FE_{H_2} was 22% (Figure S12D). The current density values recorded for

the $Au_{50}Pb_{50}$ catalyst at different potentials are shown in Figure 4 as an example, together with the FE values for the various products. At −1.07 V versus RHE, CH_4 with a FE of 2.8% was produced. At more negative potentials (−1.17 V vs RHE), we did not observe a further increase in FE_{CH_4}, but HER activity increased. Three parallel long-term electrolysis experiments were carried out at −1.07 V versus RHE (see an example in Figure 4C). A stable current of −10.8 ± 0.5 mA cm^{-2} was achieved with CO, HCOOH, and CH_4 FEs of 25.7 ± 8.0, 25.5 ± 0.7, and 2.8 ± 0.4%, respectively, during the 3 h electrolysis. Smaller FE values were seen at the same potential for the $Au_{50}Pb_{50}$ catalyst heated in Ar (with the parallel rise of the competing HER) for all CO_2R reduction products (Figure S13). By changing the composition to $Pb_{95}Au_5$ (Figure S14A,B), low current densities <−0.5 mA cm^{-2} were achieved in the lower cathodic potential region (−0.77 to −0.87 V vs RHE), associated mainly with HER. At potentials more negative than −0.87 V versus RHE, not only the FE_{HCOOH} was increased but also CH_4 was produced with 4.8% FE, achieving a FE_{tot} of ~100% (at −1.07 V vs RHE). For Au_5Pb_{95} and $Au_{20}Pb_{80}$ catalysts (Figure S14C,D), CO was generated with a FE of 1−2% at different potentials. FE_{HCOOH} increased with increasing potentials, but H_2 evolution exhibited an opposite trend on the Au_5Pb_{95} electrode. $Au_{20}Pb_{80}$ electrode shows very little dependence of the potential. CH_4 was not detected at potentials less negative than −1.07 V versus RHE.

To investigate the effect of electrode composition (especially on CH_4 formation which represents the reduction process that requires the transfer of eight electrons), we compared the product distribution and partial current densities during CO_2 electrolysis at −1.07 V versus RHE. A relatively stable current

Figure 5. Electrochemical CO_2 reduction activity of the Au–Pb catalysts at −1.07 V vs RHE: (A) Total current density and (B) partial current density of CH_4 as a function of composition. Partial current density of H_2, CO, and HCOOH on (C) air-heated catalysts and (D) Ar-heated samples.
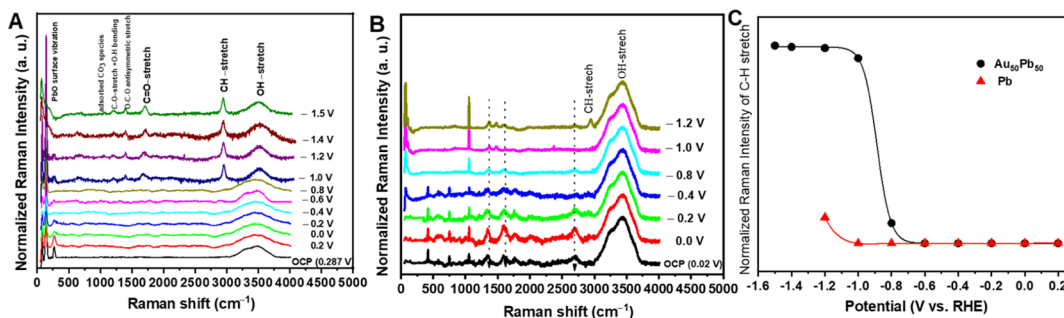
Figure 6. Raman spectra collected in CO_2-saturated 0.5 M $KHCO_3$ as a function of the applied potential (A) on the $Au_{50}Pb_{50}$ catalyst and (B) on pure Pb (dotted lines mark the bands from the substrate). (C) Potential dependence of (C–H-stretch) intensity of formate anion at 2950 cm^{-1} on $Au_{50}Pb_{50}$ and Pb NPs as a function of the applied potential. The potential is versus RHE scale.

density was measured in all cases, and its value increased with the Au content (Figures 5A and S15). The partial current density for CO production reached −3.2 mA cm^{-2} on $Au_{50}Pb_{50}$ heated in air (Figure 5C), whereas for the other catalysts, the CO formation dropped to ∼−0.16 mA cm^{-2}. j_{H_2} declined linearly with increasing Pb content, which is characteristic of Pb.[51] j_{CH_4} increased from −0.15 to −0.16, −0.24, and −0.33 mA cm^{-2} for $Pb_{95}Au_5$, Au_5Pb_{95}, $Au_{20}Pb_{80}$, and $Au_{50}Pb_{50}$, respectively (Figure 5B). This trend suggests that comparable amounts of Au and Pb are needed at the surface to ensure high reaction rates (see also Table S1). Importantly, the formation rate of CH_4 was always higher on samples heated in air compared to their Ar-heated counterparts.

A 10 h electrolysis was performed at −1.07 V versus RHE to assess the stability of the $Au_{50}Pb_{50}$ catalyst and verify the continuous production of CH_4 (Figure S16). The total current
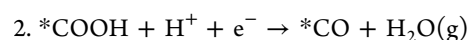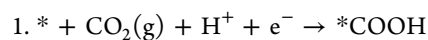
density stabilized at −13 mA cm^{-2} after 1 h and remained constant. FE_{CH_4} varied within 2.8−2.1%. We performed an additional experiment with labeled $^{13}CO_2$ and $KH^{13}CO_3$, and the almost exclusive formation of $^{13}CH_4$ was verified (deduced from the m/z = 17 signal), confirming that the detected CH_4 came from CO_2 reduction (see Figure S17 and discussion therein).

We also performed a set of controlled experiments in which the electrodes were prepared from a physical mixture of Au and Pb NPs. A physically mixed electrode (60 at. % Au + 40 at. % Pb) with a composition similar to that of the $Au_{50}Pb_{50}$ catalyst (as confirmed by EDX analysis, Table S1) was prepared and investigated at −1.07 V versus RHE (Figures S18 and 4). A current density of −6 mA cm^{-2} was achieved (note the −10.8 mA cm^{-2} value recorded for the respective bimetallic catalyst). The CO and CH_4 FEs significantly dropped to 2 and <0.5%, respectively, whereas FE_{HCOOH} increased to 50%. This suggests that the interfaces among
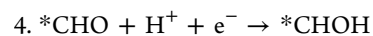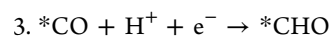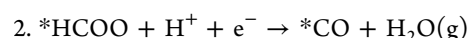
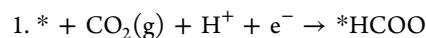the monometallic domains are the plausible active sites for CO_2 reduction to CH_4. In the Au−Pb system, the monometallic domains are more adjacent through nanostructured Au/Pb interfaces, whereas the physically mixed system contains much less interfaces. We performed a CO electrolysis experiment which yielded CH_4 with a 4.9% FE, which is comparable to that observed in CO_2 reduction. This proves that the bimetallic Au−Pb electrodes can reduce CO and suggests CO to be a key intermediate in the proposed mechanism (see Figure S19 and discussion therein).

To gain further insights into the mechanism of the CO_2 reduction process, Raman spectra were collected under electrochemical control. This allows the direct monitoring of both the changes in the chemical nature of the electrocatalysts as well as the formation of certain reaction intermediates and products during the electrolysis.[52] The spectra collected between the open circuit-potential and −0.6 V versus RHE exhibit only bands associated with tetragonal PbO (84 and ~144 cm^{-1}) and orthorhombic PbO (280 cm^{-1})[53] and the O−H stretching mode of the adsorbed water (3000−3700 cm^{-1}, this band was almost independent of the potential).[52] At a moderate negative potential (−0.8 V vs RHE), new bands appeared, and their intensities show a slight potential dependence (Figure 6A). The PbO bands became more intense and slightly shifted at more negative potentials because of the formation of surface defects as a result of partial reduction (Figure S20A).[20,54] This shift indicates that the CO_2 reduction proceeds at potentials where PbO_x is present. At potentials more negative than −1.5 V versus RHE, it was difficult to collect Raman spectra because of intense gas evolution. The bands' assignment is presented in Figure 6A and summarized in Table S2; a band at 2950 cm^{-1} and several bands of moderate intensity in the region of 900−1715 cm^{-1} were observed. These bands are similar to those observed during CO_2 reduction on Au−Sn bimetallic NPs[20] and adsorption of HCOOH on silver colloids and Cu,[55,56] indicating the formation of HCOOH and the presence of adsorbed bicarbonate species. The spectra recorded for pure Pb show the formation of $PbCO_3$ at the beginning of the experiment, and there is an instant and considerable decrease in the intensity of the PbO band (Figures 6B and S20B). Interestingly enough, PbO_x seems to be better stabilized on Au−Pb bimetallic surfaces than on pure Pb surface. This trend was already seen on the LSV traces, where the lower onset potential was observed only for those air-heated samples where higher amounts of Au were present, ensuring stability for the PbO_x phase. Furthermore, more negative potential was required for developing the bands on Pb NPs (Figure 6C), consistent with the observed trend of the onset potential (Figure 3B). The presence of strong intensity bands of the adsorbed species on the Au−Pb bimetallic surface compared to Pb NPs could be attributed to the surface-enhanced Raman scattering. This is most likely due to the presence of Au NPs, where the laser wavelength is compatible with the localized surface plasmon resonance band of Au (ref 9 in the Supporting Information).
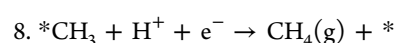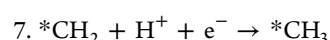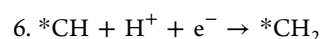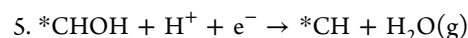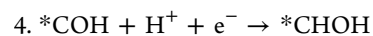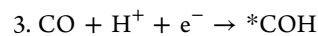
The DFT simulations were performed coupled to the Computational Hydrogen Electrode (CHE) thermodynamic model to reproduce the multiple possible paths for producing CH_4 according to the literature[15,36,57]

1. $* + CO_2(g) + H^+ + e^- \rightarrow *COOH$

2. $*COOH + H^+ + e^- \rightarrow *CO + H_2O(g)$

Alternative path for steps 1, 2

1. $* + CO_2(g) + H^+ + e^- \rightarrow *HCOO$

2. $*HCOO + H^+ + e^- \rightarrow *CO + H_2O(g)$

3. $*CO + H^+ + e^- \rightarrow *CHO$

4. $*CHO + H^+ + e^- \rightarrow *CHOH$

Alternative path for steps 3, 4

3. $CO + H^+ + e^- \rightarrow *COH$

4. $*COH + H^+ + e^- \rightarrow *CHOH$

5. $*CHOH + H^+ + e^- \rightarrow *CH + H_2O(g)$

6. $*CH + H^+ + e^- \rightarrow *CH_2$

7. $*CH_2 + H^+ + e^- \rightarrow *CH_3$

8. $*CH_3 + H^+ + e^- \rightarrow CH_4(g) + *$

where * represents the active site where the fragment is bound. After surface energy evaluations, the Au(111), Pb(111), $PbAu_2$(111), and Pb_2Au(100) surfaces were retained for reactivity evaluation as they have the lowest energy surfaces. From the simulations ran on these systems, a few general conclusions can be drawn. (1) CH_4 cannot be formed in the absence of O in the lattice because the reaction would be blocked at the first intermediate already while forming COOH or HCOO (see the analogy with the samples heat treated in Ar). (2) Without O inside the lattice, the intermediates containing O bind too strongly to Pb, and therefore the reaction cannot progress further. (3) If O is already present inside the lattice, the intermediates containing O are less bound, and the reaction can evolve toward CH_4. As seen in Table S3, the calculations performed without O have a positive ΔG at the first step (formation of COOH or HCOO). This would suggest that the inclusion of O is necessary to get through this first step. (4) If the system contains O but Au is not present, the reaction cannot proceed after the third step because the O in the lattice would capture the H of CHOH, preventing the formation of CH. This suggests that the role of Au is crucial to provide the right sites in the final steps from CH to form CH_4 that allow methane production.

As shown in the reaction profile (Figure 7, the combination of Pb, Au, and O allows the formation of CH_4 as the green path has a negative ΔG for every step and is therefore exergonic; however, this does not mean that the process has to go all the way to CH_4. The reaction can terminate early by forming HCOOH (blue path in Figure 7), which in fact was observed experimentally. It can be noticed that there is actually a more energetically favorable path to form formate (not shown in Figure 7) that involves *HCOO instead of *COOH[49] (see Table S9 in the Supporting Information).

Furthermore, the position and orientation of the intermediates during the transition from CHOH to CH are crucial. If the intermediate CHOH is too close to the O* sites on the surface, it could easily lose an H, rendering adsorbed CHO* and OH*. This would lead to an alternative CO reduction path that prevents the formation of CH_4 (red path in Figure 7). This destabilizing path is even more visible on the simulations with a larger cell in Figure S28 with an Au island because the
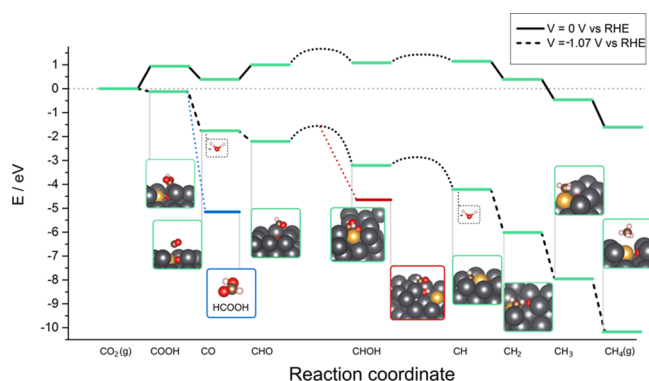
Figure 7. Energy profile on Pb—Au system with 3% Au and O impurities inside the surface. Each step involves a H$^+$ and e$^-$ transfer. In green is the full CH$_4$ path. The reaction can be stopped early in the HCOOH path in blue. The transition from CHOH to CH can be stopped if the intermediate CHOH is too close to the O site in the lattice (partial oxide phase) in the red path that could lead to CO reduction.

interface between Au and Pb can present some gaps due to the lattice mismatch between Au and Pb, making it easier intermediates to be stuck there.

In summary, the Pb(111) with O in the lattice and Au in the surrounding appearing at the interface between the Pb and Au domains is capable of forming CH$_4$, H$_2$, CO, and HCOOH as observed experimentally (see Tables S6—S9). This synergetic site allows simultaneously the first steps because the oxygen in the lattice (partial oxide) limits the formation of formate, whereas at the end of the cycle, the low adsorption of the Au sites enhances methane formation/desorption. Therefore, fine-tuning of the binding energies is needed. In our case, this was obtained by reducing the energy of oxygenated intermediates to Pb (due to the oxygen poisoning) and providing enough desorption sites in the form of Au-containing sites. Meeting all these conditions is only possible at the interface and therefore would explain the low amount of methane produced.

■ CONCLUSIONS

We have synthesized a series of Au—Pb bimetallic catalysts with different Au/Pb interfaces and studied their CO$_2$-reduction performance. The structural and composition characterizations by XRD, TEM, and XPS proved that the Au—Pb catalyst consists of Au NPs deposited on the top of Pb NPs with a native Pb oxide (PbO$_x$). These structural moieties work synergistically to transform CO$_2$ to >2e$^-$ reduction product (namely CH$_4$) on a Cu-free catalyst. The maximum CH$_4$ formation rate was 0.33 mA cm^{-2} on Au$_{50}$ Pb$_{50}$ at −1.07 V versus RHE. Control experiments on Au, Pb, or their physical mixture yielded only trace amounts of CH$_4$, further proving our notion on the role of nanoscale interfaces. In situ Raman spectroelectrochemistry confirmed the existence and stability of PbO$_x$ under the reduction conditions on the bimetallic catalyst (unlike for bare Pb), which seems to be necessary for CH$_4$ formation. We have also performed extensive DFT simulations to address the origin of the reactivity and the synergies between the different components. Pb alone overbinds the oxygen-containing intermediates. The introduction of oxygen into the structures reduces the binding energy of these intermediates. Finally, Au centers are necessary to allow the final steps in the CH$_4$ evolution.

Overall, although the partial current density and FE values are not very high, the fact that a bimetallic interface allows otherwise forbidden reaction pathways to highly reduced CO$_2$ reduction products might contribute to the rational design of complex interfaces. Furthermore, when comparing the activity descriptors (i.e., overpotentials, current density, and FE) with those of other electrocatalysts[33,35,58] that do not contain copper and demonstrate the formation of highly reduced products (see also the Introduction), we can conclude that Au—Pb catalysts are indeed very promising as Cu-free catalyst alternatives.

■ ASSOCIATED CONTENT

ⓢ Supporting Information

The Supporting Information is available free of charge at

Experimental methods, TEM and SEM images, XRD analysis, DFT energy tables, and additional electrochemical measurements (PDF)

■ AUTHOR INFORMATION

Corresponding Author

Csaba Janáky − *Department of Physical Chemistry and Materials Science, Interdisciplinary Excellence Centre, University of Szeged, Szeged H-6720, Hungary;* ⓘ orcid.org/0000-0001-5965-5173; Phone: +36-62-546-393; Email: janaky@chem.u-szeged.hu

Authors

Ahmed Mohsen Ismail − *Department of Physical Chemistry and Materials Science, Interdisciplinary Excellence Centre, University of Szeged, Szeged H-6720, Hungary; Chemistry Department, Faculty of Science, Alexandria University, 21321 Alexandria, Egypt*

Gergely F. Samu − *Department of Physical Chemistry and Materials Science, Interdisciplinary Excellence Centre, University of Szeged, Szeged H-6720, Hungary;* ⓘ orcid.org/0000-0002-3239-9154

Huu Chuong Nguyễn − *Institute of Chemical Research of Catalonia, The Barcelona Institute of Science and Technology, 43007 Tarragona, Spain*

Edit Csapó − *Department of Physical Chemistry and Materials Science, Interdisciplinary Excellence Centre, University of Szeged, Szeged H-6720, Hungary; Department of Medical Chemistry, MTA-SZTE Biomimetic Systems Research Group, Szeged H-6720, Hungary*

Núria López − *Institute of Chemical Research of Catalonia, The Barcelona Institute of Science and Technology, 43007 Tarragona, Spain;* ⓘ orcid.org/0000-0001-9150-5941

Complete contact information is available at:

■ REFERENCES

(1) Lewis, N. S.; Nocera, D. G. Powering the Planet: Chemical Challenges in Solar Energy Utilization. *Proc. Natl. Acad. Sci. U.S.A.* **2006**, *103*, 15729−15735.

(2) Song, R.-B.; Zhu, W.; Fu, J.; Chen, Y.; Liu, L.; Zhang, J. R.; Lin, Y.; Zhu, J. J. Electrode Materials Engineering in Electrocatalytic CO_2 Reduction: Energy Input and Conversion Efficiency. *Adv. Mater.* **2019**, 1903796.

(3) Turner, J. A. Realizable Renewable Energy Future. *Science* **1999**, *285*, 687−689.

(4) Whipple, D. T.; Kenis, P. J. A. Prospects of CO_2 Utilization via Direct Heterogeneous Electrochemical Reduction. *J. Phys. Chem. Lett.* **2010**, *1*, 3451−3458.

(5) Lu, Q.; Jiao, F. Electrochemical CO_2 Reduction: Electrocatalyst, Reaction Mechanism, and Process Engineering. *Nano Energy* **2016**, *29*, 439−456.

(6) Centi, G.; Quadrelli, E. A.; Perathoner, S. Catalysis for CO_2 Conversion: A Key Technology for Rapid Introduction of Renewable Energy in the Value Chain of Chemical Industries. *Energy Environ. Sci.* **2013**, *6*, 1711.

(7) Kumar, B.; Brian, J. P.; Atla, V.; Kumari, S.; Bertram, K. A.; White, R. T.; Spurgeon, J. M. New Trends in the Development of Heterogeneous Catalysts for Electrochemical CO_2 Reduction. *Catal. Today* **2016**, *270*, 19−30.

(8) Endrődi, B.; Bencsik, G.; Darvas, F.; Jones, R.; Rajeshwar, K.; Janáky, C. Continuous-Flow Electroreduction of Carbon Dioxide. *Prog. Energy Combust. Sci.* **2017**, *62*, 133−154.

(9) Zhu, W.; Michalsky, R.; Metin, Ö.; Lv, H.; Guo, S.; Wright, C. J.; Sun, X.; Peterson, A. A.; Sun, S. Monodisperse Au Nanoparticles for Selective Electrocatalytic Reduction of CO_2 to CO. *J. Am. Chem. Soc.* **2013**, *135*, 16833−16836.

(10) Chen, Y.; Li, C. W.; Kanan, M. W. Aqueous CO_2 Reduction at Very Low Overpotential on Oxide-Derived Au Nanoparticles. *J. Am. Chem. Soc.* **2012**, *134*, 19969−19972.

(11) Kim, C.; Jeon, H. S.; Eom, T.; Jee, M. S.; Kim, H.; Friend, C. M.; Min, B. K.; Hwang, Y. J. Achieving Selective and Efficient Electrocatalytic Activity for CO_2 Reduction Using Immobilized Silver Nanoparticles. *J. Am. Chem. Soc.* **2015**, *137*, 13844−13850.

(12) Chen, Y.; Kanan, M. W. Tin Oxide Dependence of the CO_2 Reduction Efficiency on Tin Electrodes and Enhanced Activity for Tin/Tin Oxide Thin-Film Catalysts. *J. Am. Chem. Soc.* **2012**, *134*, 1986−1989.

(13) Lee, C. H.; Kanan, M. W. Controlling H^+ vs CO_2 Reduction Selectivity on Pb Electrodes. *ACS Catal.* **2015**, *5*, 465−469.

(14) Hori, Y. Electrochemical CO_2 Reduction on Metal Electrodes. In *Modern Aspects of Electrochemistry*; Vayenas, C., White, R., Gamboa-Aldeco, M., Eds.; Springer: New York, 2008; Vol. *42*, pp 89−189.

(15) Kuhl, K. P.; Hatsukade, T.; Cave, E. R.; Abram, D. N.; Kibsgaard, J.; Jaramillo, T. F. Electrocatalytic Conversion of Carbon Dioxide to Methane and Methanol on Transition Metal Surfaces. *J. Am. Chem. Soc.* **2014**, *136*, 14107−14113.

(16) Janaky, C.; Hursan, D.; Endrodi, B.; Chanmanee, W.; Roy, D.; Liu, D.; de Tacconi, N. R.; Dennis, B. H.; Rajeshwar, K. Electro- and Photoreduction of Carbon Dioxide: The Twain Shall Meet at Copper Oxide/Copper Interfaces. *ACS Energy Lett.* **2016**, *1*, 332−338.

(17) Li, C. W.; Kanan, M. W. CO_2 Reduction at Low Overpotential on Cu Electrodes Resulting from the Reduction of Thick Cu_2O Films. *J. Am. Chem. Soc.* **2012**, *134*, 7231−7234.

(18) Kuhl, K. P.; Cave, E. R.; Abram, D. N.; Jaramillo, T. F. New Insights into the Electrochemical Reduction of Carbon Dioxide on Metallic Copper Surfaces. *Energy Environ. Sci.* **2012**, *5*, 7050.

(19) Nitopi, S.; Bertheussen, E.; Scott, S. B.; Liu, X.; Engstfeld, A. K.; Horch, S.; Seger, B.; Stephens, I. E. L.; Chan, K.; Hahn, C.; Nørskov, J. K.; Jaramillo, T. F.; Chorkendorff, I.; Chorkendorff, I. Progress and Perspectives of Electrochemical CO_2 Reduction on Copper in Aqueous Electrolyte. *Chem. Rev.* **2019**, *119*, 7610−7672.

(20) Ismail, A. M.; Samu, G. F.; Balog, Á.; Csapó, E.; Janáky, C. Composition-Dependent Electrocatalytic Behavior of Au−Sn Bimetallic Nanoparticles in Carbon Dioxide Reduction. *ACS Energy Lett.* **2019**, *4*, 48−53.

(21) Valenti, M.; Prasad, N. P.; Kas, R.; Bohra, D.; Ma, M.; Balasubramanian, V.; Chu, L.; Gimenez, S.; Bisquert, J.; Dam, B.; Smith, W. A. Suppressing H_2 Evolution and Promoting Selective CO_2 Electroreduction to CO at Low Overpotentials by Alloying Au with Pd. *ACS Catal.* **2019**, *9*, 3527−3536.

(22) Ismail, A. M.; Csapó, E.; Janáky, C. Correlation between the Work Function of Au−Ag Nanoalloys and Their Electrocatalytic Activity in Carbon Dioxide Reduction. *Electrochim. Acta* **2019**, *313*, 171−178.

(23) Kim, D.; Resasco, J.; Yu, Y.; Asiri, A. M.; Yang, P. Synergistic Geometric and Electronic Effects for Electrochemical Reduction of Carbon Dioxide Using Gold-Copper Bimetallic Nanoparticles. *Nat. Commun.* **2014**, *5*, 4948.

(24) Zhu, W.; Tackett, B. M.; Chen, J. G.; Jiao, F. Bimetallic Electrocatalysts for CO_2 Reduction. *Top. Curr. Chem.* **2018**, *376*, 41.

(25) Cai, Z.; Wu, Y.; Wu, Z.; Yin, L.; Weng, Z.; Zhong, Y.; Xu, W.; Sun, X.; Wang, H. Unlocking Bifunctional Electrocatalytic Activity for CO_2 Reduction Reaction by Win-Win Metal-Oxide Cooperation. *ACS Energy Lett.* **2018**, *3*, 2816−2822.

(26) He, J.; Johnson, N. J. J.; Huang, A.; Berlinguette, C. P. Electrocatalytic Alloys for CO_2 Reduction. *ChemSusChem* **2018**, *11*, 48−57.

(27) Pérez-Ramírez, J.; López, N. Strategies to Break Linear Scaling Relationships. *Nat. Catal.* **2019**, *2*, 971−976.

(28) Lee, C. W.; Yang, K. D.; Nam, D. H.; Jang, J. H.; Cho, N. H.; Im, S. W.; Nam, K. T. Defining a Materials Database for the Design of Copper Binary Alloy Catalysts for Electrochemical CO_2 Conversion. *Adv. Mater.* **2018**, *30*, 1704717.

(29) Yin, Z.; Gao, D.; Yao, S.; Zhao, B.; Cai, F.; Lin, L.; Tang, P.; Zhai, P.; Wang, G.; Ma, D.; Bao, X. Highly Selective Palladium-Copper Bimetallic Electrocatalysts for the Electrochemical Reduction of CO_2 to CO. *Nano Energy* **2016**, *27*, 35−43.

(30) Sarfraz, S.; Garcia-Esparza, A. T.; Jedidi, A.; Cavallo, L.; Takanabe, K. Cu-Sn Bimetallic Catalyst for Selective Aqueous Electroreduction of CO_2 to CO. *ACS Catal.* **2016**, *6*, 2842−2851.

(31) Jia, F.; Yu, X.; Zhang, L. Enhanced Selectivity for the Electrochemical Reduction of CO_2 to Alcohols in Aqueous Solution with Nanostructured Cu-Au Alloy as Catalyst. *J. Power Sources* **2014**, *252*, 85−89.

(32) Torelli, D. A.; Francis, S. A.; Crompton, J. C.; Javier, A.; Thompson, J. R.; Brunschwig, B. S.; Soriaga, M. P.; Lewis, N. S. Nickel−Gallium-Catalyzed Electrochemical Reduction of CO_2 to Highly Reduced Products at Low Overpotentials. *ACS Catal.* **2016**, *6*, 2100−2104.

(33) Paris, A. R.; Bocarsly, A. B. Mechanistic Insights into C2 and C3 Product Generation Using Ni_3Al and Ni_3Ga Electrocatalysts for CO_2 Reduction. *Faraday Discuss.* **2019**, *215*, 192−204.

(34) Humphrey, J. J. L.; Plana, D.; Celorrio, V.; Sadasivan, S.; Tooze, R. P.; Rodríguez, P.; Fermín, D. J. Electrochemical Reduction of Carbon Dioxide at Gold-Palladium Core-Shell Nanoparticles: Product

Distribution versus Shell Thickness. *ChemCatChem* **2016**, *8*, 952–960.

(35) Low, Q. H.; Loo, N. W. X.; Calle-Vallejo, F.; Yeo, B. S. Enhanced Electroreduction of Carbon Dioxide to Methanol Using Zinc Dendrites Pulse-Deposited on Silver Foam. *Angew. Chem., Int. Ed.* **2019**, *58*, 2256–2260.

(36) Kortlever, R.; Shen, J.; Schouten, K. J. P.; Calle-Vallejo, F.; Koper, M. T. M. Catalysts and Reaction Pathways for the Electrochemical Reduction of Carbon Dioxide. *J. Phys. Chem. Lett.* **2015**, *6*, 4073–4082.

(37) Wang, Y.; Hu, H.; Sun, Y.; Tang, Y.; Dai, L.; Hu, Q.; Fisher, A.; Yang, X. J. Facile Synthesis of Nanostructural High-Performance Cu–Pb Electrocatalysts for CO_2 Reduction. *Adv. Mater. Interfaces* **2019**, *6*, 1801200.

(38) Kresse, G.; Hafner, J. Ab Initio Molecular Dynamics for Liquid Metals. *Phys. Rev. B: Condens. Matter Mater. Phys.* **1993**, *47*, 558–561.

(39) Kresse, G.; Hafner, J. Ab Initio Molecular-Dynamics Simulation of the Liquid-Metalamorphous- Semiconductor Transition in Germanium. *Phys. Rev. B: Condens. Matter Mater. Phys.* **1994**, *49*, 14251–14269.

(40) Kresse, G.; Furthmüller, J. Efficiency of Ab-Initio Total Energy Calculations for Metals and Semiconductors Using a Plane-Wave Basis Set. *Comput. Mater. Sci.* **1996**, *6*, 15–50.

(41) Kresse, G.; Furthmüller, J. Efficient Iterative Schemes for Ab Initio Total-Energy Calculations Using a Plane-Wave Basis Set. *Phys. Rev. B: Condens. Matter Mater. Phys.* **1996**, *54*, 11169–11186.

(42) Perdew, J. P.; Burke, K.; Ernzerhof, M. Generalized Gradient Approximation Made Simple. *Phys. Rev. Lett.* **1996**, *77*, 3865–3868.

(43) Perdew, J. P.; Burke, K.; Ernzerhof, M. Generalized Gradient Approximation Made Simple [Phys. Rev. Lett. 77, 3865 (1996)]. *Phys. Rev. Lett.* **1997**, *78*, 1396.

(44) Blöchl, P. E. Projector Augmented-Wave Method. *Phys. Rev. B: Condens. Matter Mater. Phys.* **1994**, *50*, 17953–17979.

(45) Kresse, G.; Joubert, D. From Ultrasoft Pseudopotentials to the Projector Augmented-Wave Method. *Phys. Rev. B: Condens. Matter Mater. Phys.* **1999**, *59*, 1758–1775.

(46) Peterson, A. A.; Abild-Pedersen, F.; Studt, F.; Rossmeisl, J.; Nørskov, J. K. How Copper Catalyzes the Electroreduction of Carbon Dioxide into Hydrocarbon Fuels. *Energy Environ. Sci.* **2010**, *3*, 1311–1315.

(47) Nie, X.; Esopi, M. R.; Janik, M. J.; Asthagiri, A. Selectivity of CO_2 Reduction on Copper Electrodes: The Role of the Kinetics of Elementary Steps. *Angew. Chem., Int. Ed.* **2013**, *52*, 2459–2462.

(48) Nørskov, J. K.; Rossmeisl, J.; Logadottir, A.; Lindqvist, L.; Kitchin, J. R.; Bligaard, T.; Jónsson, H. Origin of the Overpotential for Oxygen Reduction at a Fuel-Cell Cathode. *J. Phys. Chem. B* **2004**, *108*, 17886–17892.

(49) García-Muelas, R.; Dattila, F.; Shinagawa, T.; Martín, A. J.; Pérez-Ramírez, J.; López, N. Origin of the Selective Electroreduction of Carbon Dioxide to Formate by Chalcogen Modified Copper. *J. Phys. Chem. Lett.* **2018**, *9*, 7153–7159.

(50) Álvarez-Moreno, M.; de Graaf, C.; López, N.; Maseras, F.; Poblet, J. M.; Bo, C. Managing the Computational Chemistry Big Data Problem: The IoChem-BD Platform. *J. Chem. Inf. Model.* **2015**, *55*, 95–103.

(51) Kim, C.; Möller, T.; Schmidt, J.; Thomas, A.; Strasser, P. Suppression of Competing Reaction Channels by Pb Adatom Decoration of Catalytically Active Cu Surfaces during CO_2 Electroreduction. *ACS Catal.* **2019**, *9*, 1482–1488.

(52) Pander, J. E.; Ren, D.; Huang, Y.; Loo, N. W. X.; Hong, S. H. L.; Yeo, B. S. Understanding the Heterogeneous Electrocatalytic Reduction of Carbon Dioxide on Oxide-Derived Catalysts. *ChemElectroChem* **2018**, *5*, 219–237.

(53) Burgio, L.; Clark, R. J. H.; Firth, S. Raman Spectroscopy as a Means for the Identification of Plattnerite (PbO_2), of Lead Pigments and of Their Degradation Products. *Analyst* **2001**, *126*, 222–227.

(54) Dutta, A.; Kuzume, A.; Kaliginedi, V.; Rahaman, M.; Sinev, I.; Ahmadi, M.; Roldán Cuenya, B.; Vesztergom, S.; Broekmann, P. Probing the Chemical State of Tin Oxide NP Catalysts during CO_2 Electroreduction: A Complementary Operando Approach. *Nano Energy* **2018**, *53*, 828–840.

(55) Castro, J. L.; Otero, J. C.; Marcos, J. I. Anomalous SERS of Monocarboxylic Acids on Silver Sols. *J. Raman Spectrosc.* **1997**, *28*, 765–769.

(56) Batista, E. A.; Temperini, M. L. A. Spectroscopic Evidences of the Presence of Hydrogenated Species on the Surface of Copper during CO_2 electroreduction at Low Cathodic Potentials. *J. Electroanal. Chem.* **2009**, *629*, 158–163.

(57) Xiao, H.; Cheng, T.; Goddard, W. A.; Sundararaman, R. Mechanistic Explanation of the pH Dependence and Onset Potentials for Hydrocarbon Products from Electrochemical Reduction of CO on Cu (111). *J. Am. Chem. Soc.* **2016**, *138*, 483–486.

(58) Kortlever, R.; Peters, I.; Balemans, C.; Kas, R.; Kwon, Y.; Mul, G.; Koper, M. T. M. Palladium-Gold Catalyst for the Electrochemical Reduction of CO_2 to C1-C5 hydrocarbons. *Chem. Commun.* **2016**, *52*, 10229–10232.